Dalton Transactions

ROYAL SOCIETY OF CHEMISTRY

PAPER

View Article Online
View Journal | View Issue

Cite this: *Dalton Trans.*, 2023, **52**, 14982

Tuning the morphology to enhance the catalytic activity of α-Ag_2WO_4 through V-doping†

Katiana Lima Patrocinio,[a] Jeziel Rodrigues Santos,[a] Luis Ignacio Granone,[b] Miguel Adolfo Ponce,[c,d] Maria Sandra Churio,[b] Lara Kelly Ribeiro,[a,e] Marcio Daldin Teodoro,[f] Rosa Llusar,[e] Juan Andrés,[e] Elson Longo[a] and Marcelo Assis *[e]

Received 24th July 2023,
Accepted 29th September 2023

DOI: 10.1039/d3dt02352d

rsc.li/dalton

Here, we present the synthesis of a highly efficient V-doped α-Ag_2WO_4 catalyst for the oxidation of sulfides to sulfones, exhibiting a high degree of tolerance towards various sensitive functional groups. Remarkably, the catalysts with 0.01% V-doping content exhibited outstanding selectivity towards the oxidation process. Scavenger experiments indicated the direct involvement of electron–hole (e^-/h^+) pairs, hydroxyl radical (•OH), and singlet oxygen ($^1O_2$) in the catalytic mechanism. Based on the experimental and theoretical results, the higher activity of the V-doped α-Ag_2WO_4 samples was associated with the preferential formation of the (100) surface in the catalyst morphology.

Introduction

In recent years, there has been significant research interest in α-silver tungstate (α-Ag_2WO_4 or AW) materials due to their multifunctionality in various fields. These materials have shown promising applications in areas such as photocatalysis,[1–3] antifungal and bactericidal agents,[4–7] tumor identification and uptake,[8,9] and gas detection.[10,11] We have recently published a comprehensive review that highlights the historical background and contemporary significance of AW-based materials, focusing on the most important properties and applications of AW-based materials.[12]

In terms of potential applications, the focus in the field of inorganic semiconductors is developing AW-based materials with enhanced catalytic activity.[13–16] A systematic study of the high catalytic efficiency of AW in the chemical fixation of CO_2 from various terminal alkynes with electron-withdrawing or electron-donating groups under atmospheric pressure was reported by Song *et al.*[17] Furthermore, Guo *et al.*[18] have employed AW as a bifunctional catalyst, enabling the simultaneous activation of CO_2 and the catalysis of direct carboxylation of terminal alkenes at room temperature. Our research group has recently demonstrated that semiconductors, including AW, exhibit remarkable efficiency and selectivity as catalysts for the dark oxidation of sulfides to sulfones.[19,20] The catalytic synthesis of sulfoxides and sulfones is of great interest due to their importance as intermediate reagents in the synthesis of various chemical and bioactive substances,[21–25] as well as for fuel desulfurization without producing harmful by-products.[26,27] For this catalytic transformation, there is a need to develop new efficient catalysts that can operate under mild conditions while maintaining high selectivity and stability.

The morphology and properties of AW are very dependent on the synthesis method and reaction conditions, such as pH, temperature, and so on.[28] For most of the applications, it is vital to have a tight control over the morphology taken by the crystals because catalytic reactions occur on the surface of semiconductors, making them surface-dependent processes. Then, tuning of the surface and morphology of efficient catalysts by controlled synthesis has become a key issue in realizing the full potential of this application. Our research group has previously reported how different solvents and surfactants in the reaction medium directly impact the final morphology of the synthesized AW microcrystals.[2,29,30] Specifically, doping processes using Zn^{2+} and Ni^{2+} metals have been found to alter the morphology of the synthesized AW samples, thereby affecting the number of active sites on the surface and conse-

[a]*CDMF-UFSCar, Universidade Federal de São Carlos, P.O. Box 676, CEP, 13565-905 São Carlos, SP, Brazil*
[b]*Departamento de Química y Bioquímica, Facultad de Ciencias Exactas y Naturales, Instituto de Investigaciones Físicas de Mar del Plata (IFIMAR), CONICET, Universidad Nacional de Mar del Plata (UNMdP), Mar del Plata, 7600, Argentina*
[c]*Instituto de Investigaciones en Ciencia y Tecnología de Materiales (INTEMA), Universidad Nacional de Mar del Plata (UNMdP), Mar del Plata, 7600, Argentina*
[d]*Physics and Engineering Research Center CIFICEN (CICPBA-CONICET), National University of the Center of the Province of Buenos Aires (UNCPBA), Tandil, B7000GHG, Argentina*
[e]*Department of Analytical and Physical Chemistry, University Jaume I (UJI), Castelló, 12071, Spain. E-mail: marcelostassis@gmail.com*
[f]*Department of Physics, Federal University of São Carlos, São Carlos, SP 13565-905, Brazil*

†Electronic supplementary information (ESI) available. See DOI: https://doi.org/10.1039/d3dt02352d

quently influencing their performance in various applications.[31,32] In this sense, vanadium doping process can emerge as an adequate strategies to control the morphology and catalytic activity of AW by changing the amount of oxygen vacancies (V_O) as well the acid characteristics of the active sites.[33–35]

In this work V-doped AW samples (x = 0, 0.01, 0.02, 0.04 mol%) were synthesized using the coprecipitation method. Various experimental techniques were employed, including X-ray diffraction (XRD) with Rietveld refinement, field emission scanning electron microscopy (FE-SEM), transmission electron microscopy (TEM), energy dispersive spectroscopy (EDS), Raman spectroscopy, diffuse reflectance spectroscopy (DRS), ultraviolet-visible reflectance spectroscopy (UV-vis), photoluminescence (PL) measurements, X-ray photoelectron spectroscopy (XPS), and electron paramagnetic resonance spectroscopy (EPR). The catalytic activity was evaluated and optimized for the oxidation of methyl phenyl sulfide (thioanisole) as a model reaction, and the performances of a series of sulfides were investigated. Density functional theory (DFT) calculations were conducted to gain a deeper understanding of the atomic-level relationship between morphology and catalysis. The predicted morphologies obtained theoretically were found to match well with the exposed surfaces observed in the electron microscopy images, providing confidence in the results. Based on the findings, we propose a mechanism to explain the changes in catalytic activity following the V-doping process, which is associated to the presence of the (100) surface in the morphology. To the best of our knowledge, no previous studies have reported on this topic, in which V is doped into AW microcrystals to enhance their efficiency as catalysts in dark conditions.

Results and discussion

Synthesis and characterization

A series of V-doped AW-based materials was synthesized using the aqueous co-precipitation method, and they were subjected to structural, morphological, and electronic analysis. To confirm the V concentration in the AW crystal lattice (in mol%), ICP-OES analyses were performed on samples digested in concentrated HNO_3, and the results are presented in Table SI-1.† The real V concentration values closely matched the expected nominal values, indicating successful doping. Fig. 1a illustrates the XRD patterns of the V-doped AW samples [0.01% (AW1 V), 0.02% (AW2 V), and 0.04% (AW4 V)] obtained through the CP method at room temperature. According to crystallographic card number 243987 in the Inorganic Crystal Structure Database (ICSD), the samples exhibit an orthorhombic structure with space group *Pn2n* and lattice parameters a = 10.8869 Å, b = 12.0400 Å, c = 5.90711, and angles $\alpha = \beta = \gamma = 90°$, with no presence of secondary phases.[32] All samples show well-defined diffraction peaks, indicating a reasonable degree of structural order and long-range crystallinity. However, Fig. 1b demonstrates that the most intense diffraction peak (231) shifts to higher 2θ values as the concentration of vanadium clusters (V-clusters) in the crystal lattice increases. This behavior can be explained by analyzing the values of the full width at half maximum (FWHM) of the peak (231).[9] The FWHM values for the samples are 0.465°, 0.379°, 0.323°, and 0.389° for AW, AW1 V, AW2 V, and AW4 V, respectively (Table SI-2†). The decrease observed in the FWHM values of AW, AW1 V, and AW2 V may be attributed to an increase in the degree at long-range structural ordering. Conversely, AW4 V exhibits the highest FWHM value among the doped samples, indicating a higher concentration of V-clusters in the lattice, causing structural reorganization and resulting in a higher degree of disorder. However, when comparing AW and AW4 V, the doped sample still demonstrates higher structural order. Therefore, the observed shift in the main peak indicates the distortions and polarization effects induced in the crystalline

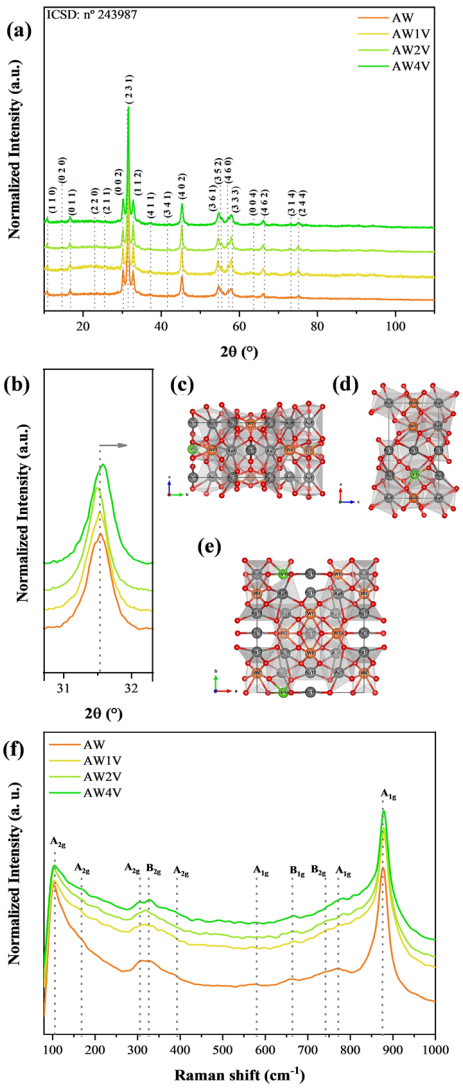

Fig. 1 (a) XRD patterns of the AW samples; (b) inset view of the main peak (231); schematic representation of the crystalline unit cell of AWV with (x = 0.125) in the coordinates a (c), b (d), and c (e). (f) Raman spectra of the samples.

lattice by the successful substitution of [WO_6] clusters with V-clusters.

The Rietveld refinement plots for the samples are presented in Fig. SI-1.† All the results exhibit excellent agreement between the experimental XRD patterns and the theoretical results based on ICSD card number 24398. The formation of V-clusters leads to a higher electron density in the lattice, resulting in an increase in the lattice parameters and volume of the crystal unit cell (see Table SI-2†). The V-doping process in the AW microcrystal lattice induces local distortions and redistribution of charge density, leading to an increase in the crystallite size (D) value of the V-doped AW samples.

Additionally, the microstrain (ε) values of the samples generally show an increase compared to the AW sample, indicating that the substitution of [WO_6] clusters with V-clusters induces structural and electronic changes in the AW crystalline lattice.[36] These modifications appear as a consequence of the structural defects and polarization caused by the formation of V-clusters, instead of an octahedral cluster [WO_6], and local variation in electron density generated in the lattice after the formation of new V–O bonds in the V-clusters. Furthermore, an increase in the crystallite size of V-doped samples is observed. Based on the theoretical model, Fig. 1c–e show that the V-cluster is surrounded by 4 oxygen atoms, forming a distorted tetrahedral cluster [VO_4].

Micro-Raman spectroscopy is a valuable technique for investigating the impact at short-range structural order/disorder in crystalline solids. As mentioned earlier in the XRD results, the samples exhibit an orthorhombic structure, and thus, 21 characteristic vibrational modes are expected, divided into two categories: internal modes (associated with the molecular vibration of the [WO_6] moiety) and external modes (attributed to the movement of the Ag^+ ion).[37–39] However, the Raman spectra reveal only 10 active modes in the range of 50 to 1000 cm^{-1} (Fig. 1f). The most prominent peak at 875 cm^{-1} (A_{1g}) corresponds to the asymmetric stretching of the O–W bonds in [WO_6]. The modes at 773 cm^{-1} (A_{1g}) and 741 cm^{-1} (B_{2g}) arise from the symmetrical elongation of W–O–O–W and W–O, respectively, while the mode at 665 cm^{-1} (B_{1g}) is associated with the symmetrical elongation of W–O–O–W. The modes at 579 cm^{-1} (A_{1g}), 385 cm^{-1} (A_{2g}), and 333 cm^{-1} (B_{2g}) are linked to the bending vibrations of the W–O–W bond angle and W–O–O–W dihedral angle. The mode at 308 cm^{-1} (A_{2g}) corresponds to the out-of-plane fold of W–O–O–W. Lastly, the modes below 251 cm^{-1} are related to the external vibrational modes between Ag^+ and WO_4^{2-} groups.[40] These findings align with the theoretically derived frequencies illustrated in Fig. SI-2 and Table SI-3.† In Fig. 1f, it can be observed that an increase in the concentration of [VO_4] clusters within the AW crystalline lattice leads to a decrease in the intensity and resolution of the modes. The substitution of [WO_6] clusters with [VO_4] clusters likely induces short-range structural ordering due to the presence of defects in the AW crystalline structure. Concerning mode definition, Gupta *et al.*[38] and Pinatti *et al.*[41] have reported that an increased concentration of Eu^{3+} in AW facilitates short-range structural organization of the doped samples, primarily due to changes in the oxygen vacancies ($V_O^{\bullet} \rightarrow V_O^{x}$ or $V_O^{\bullet} \rightarrow V_O^{\bullet\bullet}$) present in the host matrix. This phenomenon reduces material tension and, consequently, results in relaxation of the crystalline structure, leading to well-defined Raman modes.

XPS analysis was conducted to examine the oxidation states and surface composition of the synthesized samples. Fig. SI-3† shows the experimental and deconvoluted core level spectra of the Ag 3d and W 4f peaks. The two component peaks at 367 and 374.6 eV can be assigned to Ag^0 and Ag^+ states, respectively. The peak at 34.8 and 37.8 eV, along with the satellite, are associated with the presence of W^{6+} and W^{5+} states and W 2p states, respectively.[29] In the O 1s XPS spectra, different Gaussian peaks were used to distinguish between oxygen atoms bound to water and those bound to the crystalline lattice (as shown in Fig. 2a–d). The electronic density surrounding the oxygen atoms not bound to the crystalline lattice is higher compared to those in the lattice. Consequently, the charge distribution on the oxygen atoms not bound to the lattice is shifted towards the oxygen atoms, resulting in a lower nuclear potential and, hence, a lower binding energy for these electrons. As a result, the high binding energy peak at 532.07 eV and the low binding energy peak at 530.19 eV in the O 1s spectrum can be attributed to oxygen atoms bound to the crystalline lattice (O_L) and oxygen atoms not bound to the lattice, respectively.[29] The O 1s peak at 532.07 eV includes oxygen species such as W–O, Ag–O, V–O, and O–OH, with the latter representing adsorbed oxygens from water (O_W), while the 530.19 eV O 1s peak corresponds to W–O–W bonding in OL. The O 1s peak in the 532.07 eV region may also include the contribution of superficial oxygen vacancies (V_O), as it is believed that the binding energy of O 1s resulting from this bond is similar to that of other oxygen atoms not bound to the lattice. It is worth noting the presence of a component at approximately 531 eV for the V-doped samples (O_{V-O}). The percentage of deconvolution varies between 8.73, 3.8, and 12.18%. Although the intensity does not increase with increasing V-doping concentration, this component indicates the presence of connections that can occur with V–O outside the crystalline lattice.[42]

XPS, being one of the modern techniques widely used for studying the surface of solid materials, can be effectively employed to explore these doping modifications. Therefore, high-resolution analysis of the V 2p level was performed (Fig. 2e). The two-component peaks around 516 and 518 eV can be attributed to the V^{4+} and V^{5+} states, respectively. The presence of vanadium ions in the samples is evident from the increased peak in the XPS survey spectrum (see Fig. SI-4†), which is expected to increase with higher doping levels, as observed in the deconvolution of V 2p in Fig. 2e. It is also expected that this doping will modify the oxyanion lattice to form bonds such as W–O–V^{4+}.[43]

The electronic modifications caused by V doping in the AW samples were initially analyzed using DRS. The optical band gap energies (E_{gap}) were calculated from the UV-vis absorption spectra obtained from DRS using the Wood–Tauc[44] and Kubelka–Munk[45] equations AW exhibits an absorption spec-

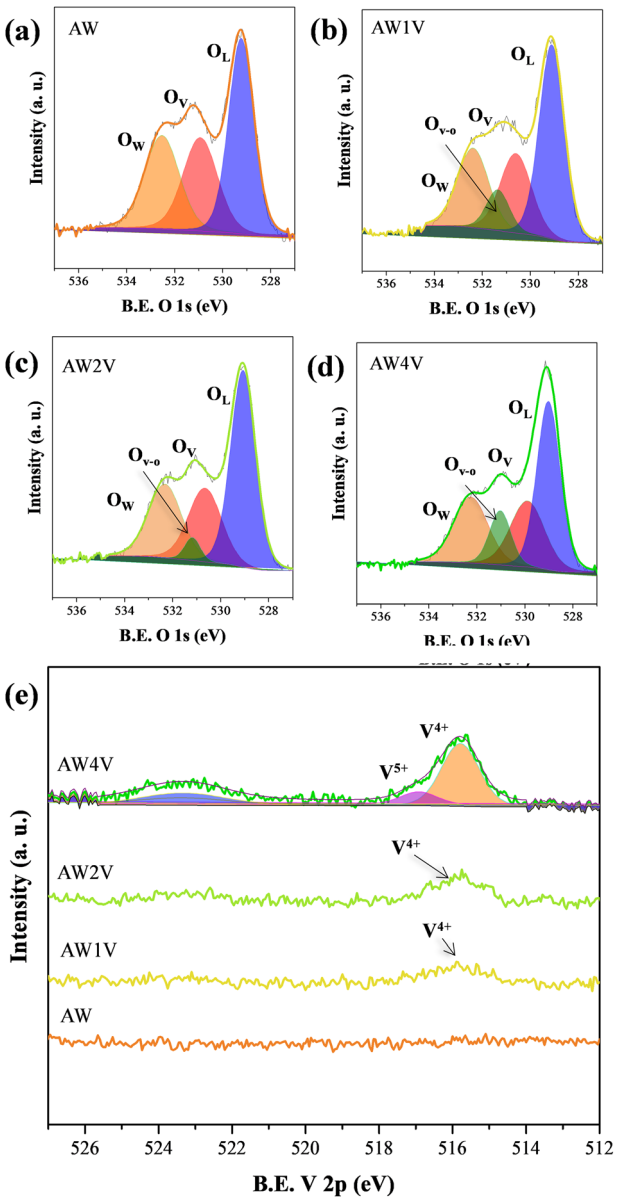

Fig. 2 (a–d) Core-level XPS spectra of O 1*s* and (e) V 2p for the samples.

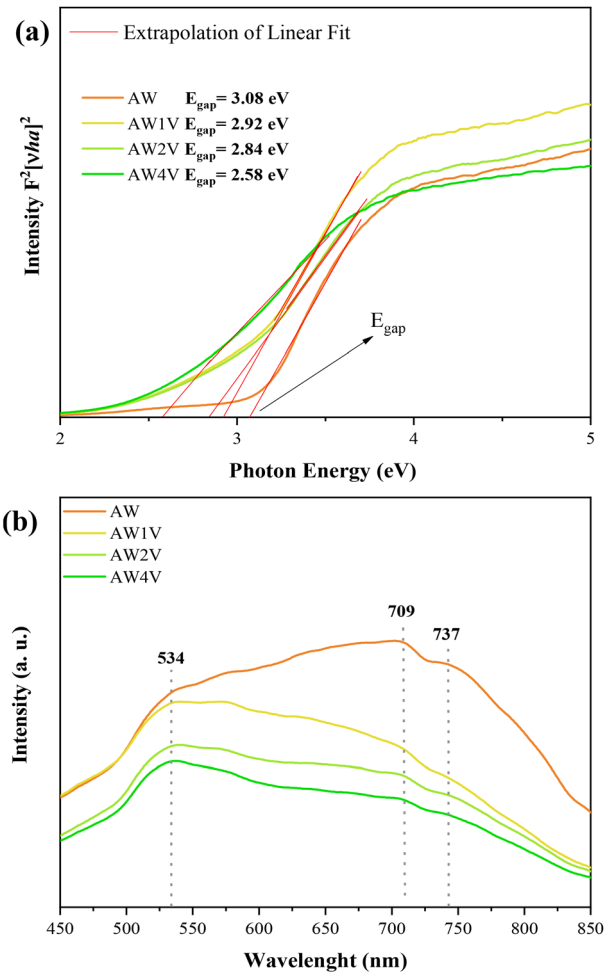

Fig. 3 (a) DRS and (b) PL spectra of the samples.

trum driven by direct electronic transitions, resulting from the movement of electrons located in the conduction band minimum energy states to the valence band's maximum energy states at different points in the Brillouin zone (Fig. 3a).[46,47] Previous studies conducted by our group using the same synthesis method reported E_{gap} values for AW between 3.08–3.18 eV,[30,32,41] which is consistent with the E_{gap} value obtained for the AW sample in this study (3.08 eV). A reduction in the E_{gap} value was observed for the V-doped samples, with values of 2.92 eV (AW1 V), 2.84 eV (AW2 V), and 2.58 eV (AW4 V). Analysis of the results indicates that as the concentration of $[VO_4]$ clusters in the AW crystalline lattice increases, there is a decrease in the E_{gap} values due to an increase in excited state electrons, which migrate from the ground state to the forbidden region of the semiconductor band gap. According to Shen *et al.*, this reduction in the band gap energy is directly related to the introduction of new electronic levels from the V 3d orbitals.[48]

PL spectroscopy was employed to evaluate the effect of substituting $[WO_6]$ with $[VO_4]$ clusters on the structure and electronic properties of the materials. This technique provides valuable information at medium-range in the material structure. The AW sample exhibits a broad emission profile, which is a result of a multiphonon process involving several intermediate states within the band gap.[36,49] This emission is associated with structural defects in the matrix and typically appears in the blue-green region, indicating charge transfer in the $[WO_6]$ clusters.[50] On the other hand, the PL emissions in the red region are attributed to extrinsic defects (such as structural order/disorder and interfaces) that are related to $[AgO_x]$ clusters (x = 2, 4, 6, and 7).[31,41] These defects induce a symmetry-breaking process, leading to polarization in the structure through charge transfer between ordered and disordered clusters. This quantum effect probabilistically forms neutral clusters as well as clusters with higher and lower charge density, generating electron–hole pairs (e^-–h^+). Fig. 3b illus-

trates the PL spectra of the samples obtained at room temperature with laser excitation at 355 nm, revealing a broad emission profile ranging from 500 to 750 nm. In the case of the AW sample, a prominent peak of PL emission is observed in the red region at 709 nm, along with a less intense shoulder in the blue-green region at 534 nm. It is noteworthy that the substitution of [WO_6] clusters with [VO_4] clusters leads to a decrease in the overall intensity of the PL emission, particularly in the red region. However, the emission in the blue-green region becomes more defined. This behavior can be correlated with the results obtained from XRD, Raman spectroscopy, and DRS analysis. The deconvolution of the PL spectra was performed into three components at 544, 661, and 754 nm in order to quantify the observed modifications in each sample (Fig. SI-5†). It was observed that the component located at 661 nm remains nearly constant in all samples, while the major changes occur in the 554 and 754 nm components, directly related to shallow defects (near the valence (VB) and conduction band (CB)) and deep defects (within the middle of the band gap) respectively.[50,51] Upon adding [VO_4] clusters, a sharp decrease in deep defects (related to extrinsic defects as mentioned earlier) occurs, leading to an increase in shallow defects. These defects are associated with a greater structural organization of AW, corroborating with the results obtained from XRD and Raman spectroscopy.

FE-SEM images were taken to investigate the structure and surface evolution of as-grown V-doped AW crystals. In Fig. 4a, it can be observed that the pure AW sample exhibits an elongated hexagonal rod morphology with preferential growth along the (010) direction, which has been previously reported.[51] However, upon V doping, a change in morphology to cobblestones is observed (Fig. 4b–d). This change can be attributed to the structural distortions and redistribution of charge density caused by the dopant, resulting in the appearance of different exposed surfaces in the morphology.[32] Additionally, the presence of [VO_4] clusters inhibits the growth of Ag nanoparticles on the surface of AW, enhancing the robustness of the samples against electron beam irradiation. The average length and width distribution of the samples were analyzed, and the histograms are presented in Fig. SI-6.† The average values of length and width were found to be 0.82 and 0.12 μm, 0.80 and 0.14 μm, 0.79 and 0.15 μm, and 0.76 and 0.16 μm for the AW, AW1 V, AW2 V, and AW4 V samples, respectively. It is worth noting that, in addition to the surface changes induced by V doping, there is a reduction in length and an increase in average width of the samples. From the EDS mapping of the samples (Fig. SI-7†), we were able to observe the homogeneous distribution of V throughout the sample, reinforcing that the doping occurred efficiently. TEM analyses were conducted; however, due to the high instability of the samples under high-energy electron beams, it was not possible to analyze the influence of V-doping on the interplanar planes of AW. Instead, it was possible to observe crystalline planes related to cubic Ag, attributable to the reduction of [AgO_x] clusters (x = 2, 4, 6, and 7), and a few planes related to AW (Fig. SI-8†).

To gain a deeper understanding of the relationship between morphology and catalytic activity, it is crucial to investigate the active sites on the exposed surfaces at the atomic and molecular levels. In our pursuit of this objective, we have published several works that utilize first-principles calculations to determine the surface energy values (E_{surf}) of each exposed surface in the crystal morphology. These calculations are combined with the Wulff construction and experimental findings based on FE-SEM images. This approach enables us not only to predict the available morphologies of a solid material but also to provide profound insights into the electronic, structural, and energetic properties that govern the final morphology of the synthesized materials.[52–55]

The investigation of the crystal surface and morphology evolution in V-doped AW samples was conducted by calculating a reaction path throughout the synthesis progress. Fig. 5 illustrates the steps required to achieve the experimental FE-SEM morphology (hexagonal rod) observed in pure AW starting from the ideal morphology. In order to obtain morphology A, the values of E_{surf} for the (010), (100), and (110) surfaces need to be increased, while the value of E_{surf} for the (001) and (101) surfaces should be decreased. Subsequently, morphology B can be derived from morphology A by further increasing the values of E_{surf} for the (010) and (110) surfaces. To match the experimental morphology observed in V-doped samples, an increase in the values of E_{surf} for the (010) and (110) surfaces, along with a decrease in the value of E_{surf} for the (101) surface, is necessary. The hexagonal rod morphology of AW is primarily composed of the (100) surface, accounting for 72.9% of the surface contribution, while the (001) and (010) surfaces contribute 19.7% and 7.4%, respectively. When AW is doped with V, changes in the experimental morphology are observed, resulting in a cobblestone morphology with equal exposure of the (100) and (001) surfaces (46.7% each), while the (010) surface exhibits a lower proportion (6.6%). Therefore, the V-doping process promotes the stabilization of the (100) surface and the destabilization of the (101) surface. This morphology has a lower E_{poly} value compared to the ideal

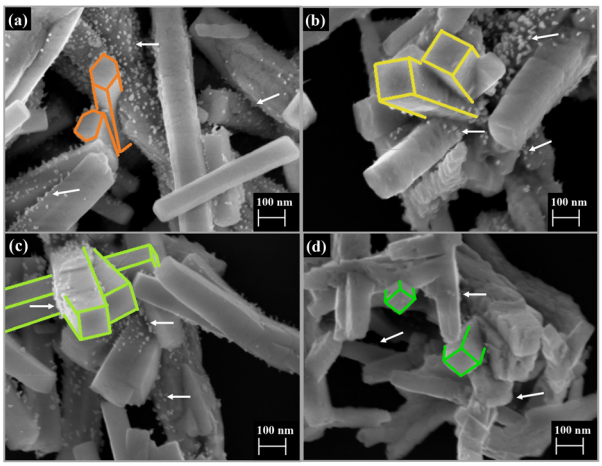

Fig. 4 FE-SEM images for (a) AW, (b) AW1 V, (c) AW2 V, and (d) AW4Vsamples.

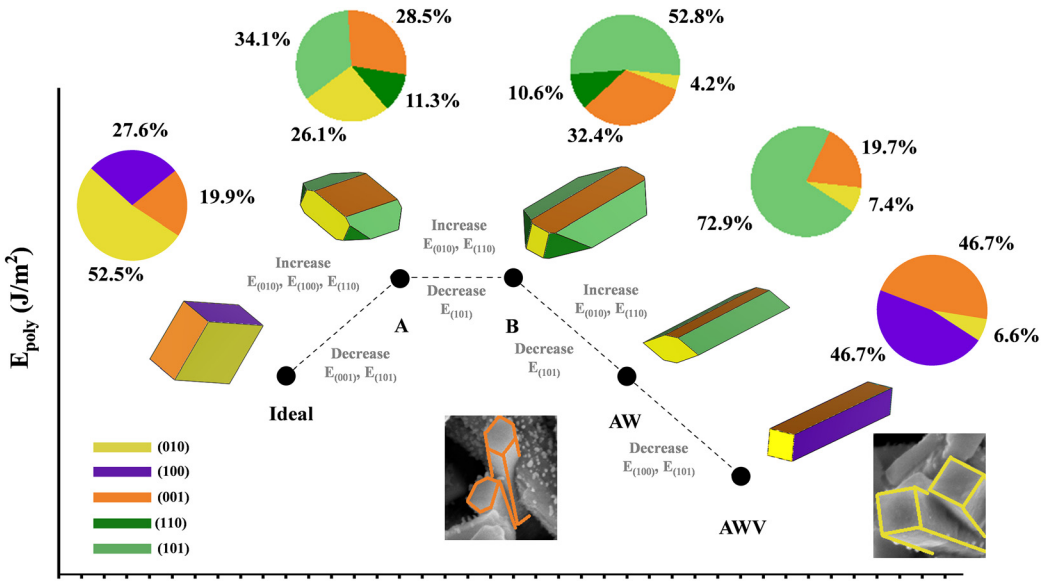

Fig. 5 Schematic representation of the energy profile to obtain the as-synthetized morphologies. The experimental morphologies are inserted for comparison purpose.

AW morphology (Table SI-4†), indicating that the high catalytic activity of the V-doped catalysts is associated with the predominant presence of the (100) surface in the morphology. These findings not only provide insights into the measured catalytic activity but also elucidate the relationship between morphology and catalysis.

EPR spectroscopy was conducted to investigate the presence of paramagnetic species in the samples. It is not expected for chemically pure and stoichiometric V-doped AW to exhibit any EPR signal since Ag^{+} ([Kr] 3d10), W^{6+} ([Xe] 4f14), and V^{5+} ([Ar]) cations do not possess unpaired electrons and are thus EPR silent. However, as discussed earlier, the introduction of V into the AW microcrystal lattice leads to intrinsic defects, local distortions, and redistribution of charge densities, which may facilitate the formation of paramagnetic centers detectable by EPR, such as oxygen vacancies, W^{5+} ([Xe] 4f14 5d1), and V^{4+} ([Ar] 3d1) cations, among other species. Fig. 6 illustrates the EPR spectra of undoped and V-doped AW samples.

It is widely recognized that semiconductor metal oxides commonly possess surface oxygen vacancies and intrinsic defects.[56] Our research group has previously investigated the nature of defects in AW.[51,57] Experimental and theoretical studies have indicated that the formation of oxygen vacancies, including neutral (neutral (V_O^x), cationic ($V_O^{\bullet}$) or doubly-ionized $V_O^{\bullet\bullet}$), is favored in both undoped and V-doped AW samples. Considering the aforementioned reactions, it is possible that in V-doped AW microcrystals, where the lowest energy level of the conduction band is associated with V 3d orbitals, electrons can transfer from V_O^x to EPR-silent V^{5+}, resulting in the generation of paramagnetic V^{4+} and $V_O^{\bullet}$ species.

Based on the preceding discussion, we can assign the observed EPR signals to specific paramagnetic species. It is important to note that trapped electrons in $V_O^{\bullet}$ exhibit an EPR response similar to that of free electrons, as extensively documented in the scientific literature for various semiconductor metal oxides.[58] Therefore, $V_O^{\bullet}$ are characterized by a pronounced resonance at *ca.* g = 2.003, as it has been widely described in the scientific literature for different semiconductor metal oxides.[58–61] However, it has been reported that oxygen vacancies in $WO_{(3-x)}$ can resonate at much higher g values. Qian *et al.*[62] and Shen *et al.*[63] detected a sharp EPR signal at g = 2.28 in a series of $WO_{(3-x)}$ samples. The authors observed that the signal intensity increases with higher x values, indicating a higher concentration of oxygen vacancies. Additionally, the signal was absent in a stoichiometric WO_3 sample, leading the authors to attribute it to the oxygen vacancies present in $WO_{(3-x)}$. Theoretical calculations conducted by Di Valentin and Pacchioni[64] demonstrated that the majority of electronic density arising from excess electrons due to an oxygen vacancy is localized at the V_O void in $WO_{(3-x)}$.

Qian *et al.* proposed that the shift in the g value from approximately 2.003 to 2.28 is attributed to the presence of two charge centers (unpaired electrons) trapped in neutral oxygen vacancies.[62] The EPR signal observed at g = 2.260 for the AW1 V microcrystals exhibits similar shape and g value to the signal associated with oxygen vacancies in $WO_{(3-x)}$. The most common defect in AW microcrystals is the Ag–O vacancy complex (V_{AG-O}), which consists of two cationic oxygen vacancies surrounding one anionic silver vacancy. In this case, the defect complex contains more than one unpaired electron, representing negatively charged centers. Therefore, the EPR signal observed at g = 2.260 for the AW1 V sample could reasonably be attributed to the Ag–O vacancy complexes. A detailed analysis of the morphological transformation is performed to answer this question: why such a signal is not observed for more highly doped or undoped samples? The (010) and (001) surfaces are common in the mor-

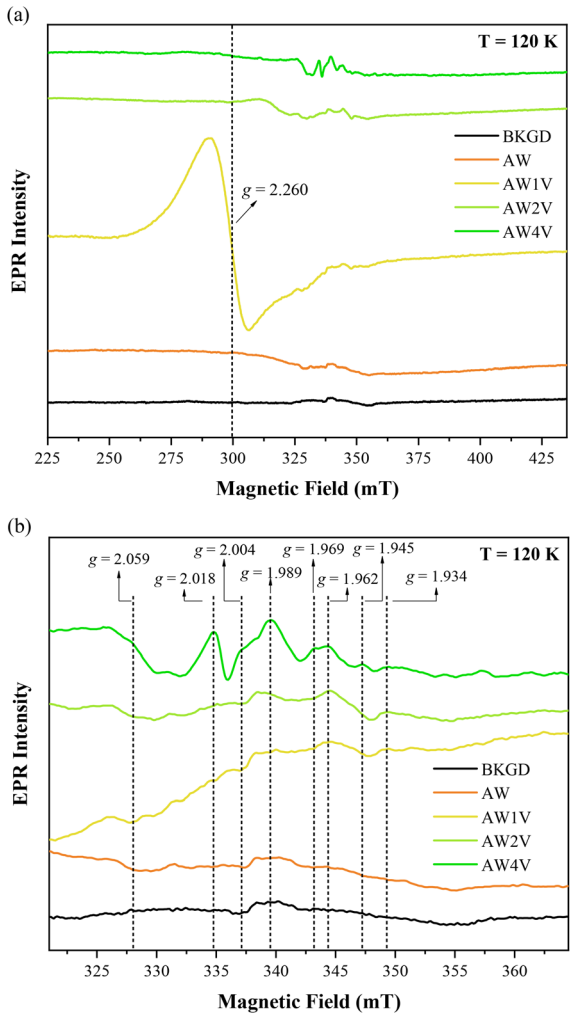

Fig. 6 X-band EPR spectra of the undoped (AW) and V-doped (AW1 V, AW2 V, and AW4 V) samples recorded at 120 K. (a) Magnetic field swept from 225 to 435 mT. (b) Magnetic field swept from 320 to 365 mT. The background spectrum (BKGD) was obtained by measuring an empty sample tube.

phology of both samples; the difference is the presence (110) and (100) surfaces. The (100) surface is composed by $[AgO_5{\cdot}2V_O]$ and $[WO_4{\cdot}2V_O]$ clusters, while the (110) surface displays the $[AgO_3{\cdot}4V_O]$, $[AgO_2{\cdot}2V_O]$, and $[WO_4{\cdot}2V_O]$ clusters.[30] Therefore, the EPR signal observed at g = 2.260 is most likely associated to the $[AgO_5{\cdot}2V_O]$ clusters, which are predominantly present in the AW1 V sample.

The observed g values ranging from 1.934 to 2.059, distinct from those observed in the AW4 V sample, are characteristic of V^{4+} ([Ar] 3d1, S = 1/2, I = 7/2) species.[65,66] These signals result from the interaction between the single electron of V^{4+} 3d1 (S = 1/2) and its nucleus (I = 7/2). Based on the micro-Raman and PL measurements, the substitution of $[WO_6]$ clusters with $[VO_4]$ clusters induces a short-range structural ordering that leads to the transformation of cationic oxygen vacancies into doubly-ionized oxygen vacancies ($V_O^{\bullet} \rightarrow V_O^{\bullet\bullet}$). In V-doped AW samples, the formation of doubly-ionized oxygen vacancies involves the transfer of the unpaired electron from a cationic oxygen vacancy to the V 3d orbitals (located at the bottom of the conduction band). Doubly-ionized oxygen vacancies do not exhibit EPR signals, which explains the absence of the signal attributed to cationic oxygen vacancies (g = 2.260) in the AW2 V and AW4 V samples. However, paramagnetic V^{4+} species are indeed detected. Therefore, the increasing intensity of the V^{4+} signals with higher doping levels (Fig. 6b) strongly supports the hypothesis that short-range structural ordering occurs in the V-doped samples.

Catalytic performance and mechanistic insights

The catalytic oxidation of sulfides using the aforementioned V-doped AW samples was investigated to analyze the impact of catalyst structure, morphology, and electronic properties on catalytic activity. Thioanisole oxidation was chosen as the model reaction (Fig. 7a). The oxidation occurs in two sequential steps, starting with the conversion of the sulfide to methyl phenyl sulfoxide, followed by further oxidation to methyl phenyl sulfone.

To assess the catalytic activity, initial experiments were conducted using the same conditions employed for the catalytic oxidation of sulfides using transition metal tungstates (2 mL CH_3CN, 50 °C, 30 min, 100 μL of H_2O_2, and 10 mg of catalyst).[19] Under these conditions, the catalytic activity of the aforementioned materials was evaluated (Fig. 7b). The AW sample exhibited a conversion of >99%, with 87% selectivity towards the sulfone product. Similarly, the AW1 V sample demonstrated a conversion of >99% with complete selectivity for the sulfone. However, the AW2 V and AW4 V samples showed decreased conversion rates of 93% and 85%, respectively, with selectivity values of 79% and 62% for sulfones. These results indicate that low concentrations of V doping in the AW crystal lattice enhance conversion and selectivity towards the final product in shorter reaction times. Although samples with lower V doping concentrations (0.5 and 0.25 mol%) were also synthesized, the AW1 V sample still exhibited the highest conversion and selectivity.

Kinetic analysis of thioanisole oxidation products was performed for the AW and AW1 V samples (Fig. 7c). It is well-documented in the literature that the initial oxidation step leading to sulfoxide formation is more facile, whereas the subsequent oxidation step for sulfone formation is more challenging to achieve.[67] Within the first 10 minutes of the reaction, the AW catalyst achieved a conversion of >99% with 62% selectivity for sulfone, while the AW1 V catalyst exhibited the same conversion with 74% selectivity for sulfone. After 30 minutes of reaction, the AW catalyst showed 87% selectivity for sulfone, whereas the AW1 V catalyst achieved >99% selectivity for sulfone.

According to Radko *et al.*,[35] the introduction of small concentrations of V doping creates new oxidation sites on the catalyst's surface, thereby significantly improving the efficiency of the process. The alterations in morphology and the subsequent stabilization of specific surface facets lead to modifications in the active sites of the material. As previously mentioned, the AW1 V sample stabilizes the (100) surface, charac-

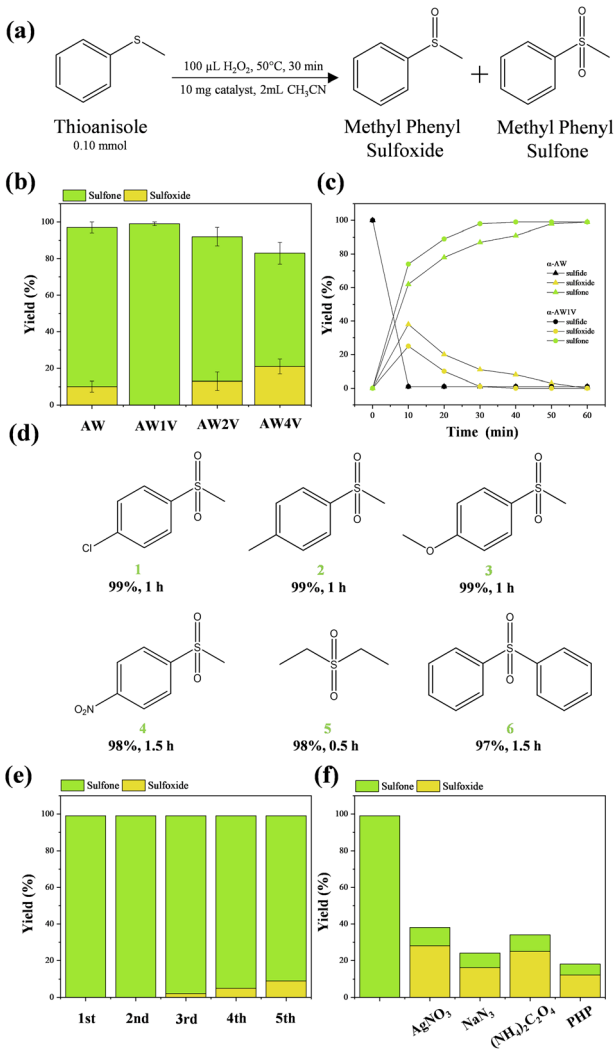

Fig. 7 (a) Thioanisole oxidation reaction scheme; (b) conversion and selectivity of different catalysts to thioanisole oxidation; (c) kinetic profile of the thioanisole oxidation for AW and AW1 V samples; (d) catalytic scope using AW1 V catalyst; (e) 10-fold scaled catalytic recycle for the oxidation reaction using AW1 V catalyst; (f) scavenger tests in the oxidation reaction using AW1 V catalyst.

terized by undercoordinated clusters [$AgO_5{\cdot}2V_O$], which serve as highly active sites responsible for the enhancement of catalytic oxidation processes. Additionally, another influential factor in catalytic activity may be the role played by V 3d orbitals in generating reactive oxygen species (ROS), which are responsible for the sulfide oxidation. It is evident that achieving a delicate balance among structural, morphological, and electronic properties is paramount in the development of novel catalysts.

With the optimal conditions established for sulfide oxidation using the AW1 V sample, sulfides with different substituents were tested to assess the system tolerance. Substituted *p*-thioanisole derivatives bearing –Cl, $–CH_3$, $–OCH_3$, and $–NO_2$ groups were successfully oxidized with excellent selectivity (Fig. 7d, **1–4**). Aliphatic thioethers were readily transformed into their respective sulfones (Fig. 7d, **5**). However, symmetric aromatic sulfides exhibited lower tolerance under the established conditions. (Fig. 7d, **6**) Finally, recycling experiments were conducted (Fig. 7e). The catalytic system remained active throughout the five tested cycles; however, a slight loss of activity was observed after the fourth cycle, with sulfone conversion reaching 91%. This deactivation of the material may be due to the degradation of the structural and surface catalyst, which can lead to the leaching of its constituent ionic species. To rule out the participation of ionic species (Ag^+, VO_4^{3-}, and WO_4^{2-}) during the recycling experiments, they were tested in the catalytic reaction. The obtained results were similar to those obtained with pure H_2O_2 (total conversion <30%), indicating that even if these species leach into the solution, they are not active for this reaction. Through XRD analysis of the sample after catalytic recycling, it is possible to observe that no secondary crystalline phases appear, and not significative changes in the intensity and position of the XRD peaks (Fig. SI-9†). However, when analyzing SEM images after recycling (Fig. SI-9†), a high agglomeration of particles can be observed, along with degradation of their initial morphology, which directly impacts their catalytic response.

The oxidation mechanism was investigated by adding equimolar amounts of scavengers for e^-, h^+, $^{\bullet}OH$ radical, and $^1O_2$ in the reaction (Fig. 7f). A significant reduction in catalytic efficiency was observed for all scavengers, indicating that these species are directly involved in the oxidation process. The mechanism of sulfide oxidation by AW involves the electronic thermo-excitation of e^- from the VB to the C to generate e^-–h^+ pairs.[19] These charge carriers diffuse to the AW surface to generate ROS responsible for the initiation of different advanced oxidation processes. H_2O_2 when in contact with the AW surface can decompose to form two $^{\bullet}OH$ radicals. On the other hand, H_2O molecule interacts with the h^+ to render $^{\bullet}OH$, while the O_2 molecules will interact with the e^- to initially transform to the superoxide radical ($^{\bullet}O_2$), which can lose an electron to form the singlet molecular oxygen, $^1O_2$[68,69] These species are potent oxidants that readily oxidize sulfides to sulfones by accessing reaction pathways with lower activation barriers.[70] The oxidation of sulfides to form sulfones through $^{\bullet}OH$ and $^1O_2$ involves their addition to the sulfur atom, followed by subsequent eliminations of H_2O and O_2, initially resulting in the sulfoxide and then, after a second oxidation step, the sulfone.[20] These findings demonstrate the occurrence of electron transfer reactions involving these short-lived species and establish parallels with the photoinduced reactions, suggesting this state as a reference system for excited-state structures and as a framework for exploring catalytic reactions.

Experimental

Synthesis of the V-doped AW samples

The V-doped AW samples were synthesized using the coprecipitation method (CP) in an aqueous medium. For the pure sample, two separate aqueous solutions were prepared: one

containing $Na_2WO_4{\cdot}2H_2O$ (0.001 M, Sigma-Aldrich, 99.5%), and the other containing $AgNO_3$ (0.002 M, Sigma-Aldrich, 99.8%). These solutions were mixed under constant agitation and heated to 70 °C, after which the $AgNO_3$ solution was added to the $Na_2WO_4{\cdot}2H_2O$ solution. This resulted in the formation of a suspension, which was stirred at a constant temperature for 20 minutes, leading to the formation of a white precipitate. The precipitate was then washed multiple times with deionized H_2O and centrifuged to remove any residual ions. For the V-doped samples, the synthesis process was similar, with the only difference being the use of two aqueous solutions: NH_4VO_3 (0.002 M, Sigma-Aldrich, 99%) and $AgNO_3$ (0.002 M, Sigma-Aldrich, 99.8%). These solutions were mixed under agitation and heated to 70 °C. In the NH_4VO_3 solution, $Na_2WO_4{\cdot}2H_2O$ (0.001 M) was added under agitation, followed by the addition of the $AgNO_3$ solution. Upon addition, a yellow precipitate was obtained.

Catalytic oxidation of sulfides

The catalytic tests were carried out in mL round-bottom flasks with magnetic stirring at 700 rpm per min. The experimental procedure involved dispersing AW sample in a mixture of 0.1 mmol of sulfide, 2 mL of solvent, and 15 μL of hexadecane as an internal standard. Then, H_2O_2 was added as the oxidant. The reaction conditions, including time, temperature, H_2O_2 amount, solvent, and catalyst loading, were varied to optimize the yield and selectivity for the transformation to sulfoxide and sulfone. The reaction solutions were diluted in 2 mL of ethyl acetate and analyzed by gas chromatography (GC, Agilent 8860) with flame-ionization detection (FID), using a non-polar (5%-phenyl)-methylpolysiloxane column (Agilent J&W HP-5). For catalytic recycles (up to 5 recycles), the experiment was scaled up by a factor of 10 under the best conditions. The experiments with ionic species were conducted using equimolar amounts of $AgNO_3$, NH_4VO_3, and $Na_2WO_4{\cdot}2H_2O$. For experiments using scavengers, equimolar amounts of reagents and catalyst were used. The scavengers used were $AgNO_3$ to capture electrons (e^-), ammonium oxalate ($(NH_4)_2C_2O_4$) for holes (h^+), potassium hydrogen phthalate (PHP) for hydroxyl radicals ($^{\bullet}OH$), and sodium azide (NaN_3) for singlet oxygen ($^1O_2$).

Characterizations

The catalysts underwent structural characterization using various techniques. XRD analysis was performed using a DMax2500PC diffractometer (Rigaku, Japan). Raman spectroscopy, conducted with a T64000 spectrometer (Horiba Jobin–Yvon, Japan) coupled with a CCD Synapse and an argon-ion laser detector operating at 514 nm, provided structural information. DRS measurements were carried out using a Varian Cary 5G spectrophotometer (Agilent, USA) equipped with an integrating sphere, and magnesium oxide (MgO) served as the reference material. PL spectra were obtained using a laser (Cobolt/Zouk; λ = 355 nm) with an incident potency of 50 μW focused on the 20 μm position. XPS analyses were performed using an ESCA spectrometer (Scientia Omicron, Germany) with a monochromatic X-ray source of Al Kα (1486.7 eV), and the binding energies of all elements were calibrated with respect to the C 1s peak at 284.8 eV. Backscattered luminescence was captured using a 20 cm spectrometer (Andor Technologies, UK) with the signal detected by a charge-coupled device detector. The morphologies and textures of the catalyst were observed using FE-SEM with a Supra 35-VP operated at 10 kV (Carl Zeiss, Germany). The EDS mapping analysis was performed using a TM4000 II Benchtop SEM (Hitachi, Japan). TEM images were obtained using an FEI TECNAI F20 microscope operating at 200 kV. Inductively coupled plasma optical emission spectrometry (ICP-OES) was employed to estimate the chemical composition of the solutions during catalytic cycles, employing an iCAP 7000 instrument (Thermo Fisher Scientific, USA). EPR spectra were acquired at 120 K using a spectrometer model ELEXSYS E500T (Bruker, Germany) equipped with an ER 4102ST rectangular resonator operating in the TE102 mode at a frequency of 9.8 GHz (X-band) and an ER 4131VT variable temperature accessory. The data acquisition parameters used for the measurements were 100.00 kHz modulation frequency, 1.00 mT modulation amplitude, 20.4 mW microwave power, 330 mT central field, 210 mT sweep width, and 20.48 ms conversion time. A total of 4096 data points were collected per scan, and the resulting spectra were the average of 5 scans.

Conclusions

Here, we present a protocol for synthesizing highly active and selective α-Ag_2WO_4 catalysts for the oxidation of sulfides to sulfones in the absence of light, based on the doping process of α-Ag_2WO_4 with vanadium. This approach effectively improves its performance for this transformation under mild conditions and selectively oxidizes various classes of sulfides. Furthermore, we demonstrate how changes in the exposed surfaces and morphology can modulate the selectivity of the V-doped α-Ag_2WO_4 samples.

The main conclusions of this work can be summarized as follows: (i) the V-doped α-Ag_2WO_4 catalyst exhibits higher efficiency for the oxidation of sulfides to sulfones compared to undoped AW; (ii) high yields and selectivity for different types of sulfones were achieved within a relatively short reaction time. The kinetic study of the 0.01% V sample showed >99% selectivity for sulfones after 30 minutes of reaction, while the undoped sample exhibited 87% selectivity. The catalyst also displayed good stability with only a 9% loss of activity after the fifth recycle; (iii) based on the above results, we propose that by adjusting the morphology (with the (100) surface being the most favorable), the catalytic activity of the material can be maximized; (iv) the results of scavenger experiments suggest a mechanism for the efficient oxidation reaction involving the presence of electron–hole (e^-–h^+) pairs, hydroxyl radicals ($^{\bullet}OH$), and singlet oxygen ($^1O_2$); (v) EPR and XPS measurements confirmed the characteristic signal of V^{4+} cations in the doped samples.

The obtained results promote V-doped α-Ag_2WO_4 material as a promising catalyst for an advanced oxidation process,

emphasizing the relationship between morphology and catalytic activity. Our findings have the potential to inspire new ideas and establish a foundation for the development of catalysts for the light-independent oxidation of sulfides to sulfones. It is hoped that these challenges can be solved in the future and the results presented here could serve as a good reference for other researchers dealing with the catalytic activity facilitated by doping and pave the way for advancements in this field.

Author contributions

K. L. Patrocinio: writing – original draft, formal analysis, methodology, investigation. J. R. Santos: formal analysis, methodology. L. I. Granone: formal analysis, methodology, writing – original draft. M. A. Ponce: methodology. M. S. Churio: methodology, resources. L. K. Ribeiro: formal analysis, methodology. M. D. Teodoro: formal analysis, methodology. R. Llusar: methodology, resources, funding acquisition. J. Andrés: writing – original draft, writing – review & editing, resources, funding acquisition. E. Longo: writing – original draft, conceptualization, writing – review & editing, resources, supervision, funding acquisition. M. Assis: writing – original draft, conceptualization, writing – review & editing, investigation, resources, supervision, funding acquisition.

Conflicts of interest

There are no conflicts to declare.

Acknowledgements

This work was partially funded by the Fundação de Amparo à Pesquisa do Estado de São Paulo – FAPESP (FAPESP CEPID-finance code 2013/07296–2), Financiadora de Estudos e Projetos – FINEP, Conselho Nacional de Desenvolvimento Científico e Tecnológico – CNPq, and Coordenação de Aperfeiçoamento de Pessoal de Nível Superior – CAPES (finance code 001). J. A. and R. L. acknowledge the Universitat Jaume I (finance codes UJI-B2022-56 and UJI-B2019-30) and Generalitat Valenciana (finance code CIAICO2021/122) for financially supporting this research. M. A. was supported by the Margarita Salas postdoctoral contract MGS/2021/21 (UP2021-021) financed by the European Union-Next Generation EU. M. S. C. and L. I. G. thank the Consejo Nacional de Investigaciones Científicas y Técnicas (Argentina) for financial contributions from PUE 22920200100016CO-IFIMAR.

References

1 L. O. Laier, M. Assis, C. C. Foggi, A. F. Gouveia, C. E. Vergani, L. C. L. Santana, L. S. Cavalcante, J. Andrés and E. Longo, Surface-Dependent Properties of α-Ag_2WO_4: A Joint Experimental and Theoretical Investigation, *Theor. Chem. Acc.*, 2020, **139**(7), 108.

2 L. Cruz, M. M. Teixeira, V. Teodoro, N. Jacomaci, L. O. Laier, M. Assis, N. G. Macedo, A. C. M. Tello, L. F. da Silva, G. E. Marques, M. A. Zaghete, M. D. Teodoro and E. Longo, Multi-Dimensional Architecture of Ag/α-Ag_2WO_4 Crystals: Insights into Microstructural, Morphological, and Photoluminescence Properties, *CrystEngComm*, 2020, **22**(45), 7903–7917.

3 M. M. Mohamed and H. El-Farsy, Rapid Reduction of Nitroarenes Photocatalyzed by an Innovative Mn_3O_4/α-Ag_2WO_4 Nanoparticles, *Sci. Rep.*, 2020, **10**(1), 21495.

4 V. M. Longo, C. C. De Foggi, M. M. Ferrer, A. F. Gouveia, R. S. André, W. Avansi, C. E. Vergani, A. L. Machado, J. Andrés, L. S. Cavalcante, A. C. Hernandes and E. Longo, Potentiated Electron Transference in α-Ag_2WO_4 Microcrystals with Ag Nanofilaments as Microbial Agent, *J. Phys. Chem. A*, 2014, **118**(31), 5769–5778.

5 F. X. Nobre, I. S. Bastos, R. O. dos Santos Fontenelle, E. A. A. Júnior, M. L. Takeno, L. Manzato, J. M. E. de Matos, P. P. Orlandi, J. de Fátima Souza Mendes, W. R. Brito and P. R. da Costa Couceiro, Antimicrobial Properties of α-Ag_2WO_4 Rod-like Microcrystals Synthesized by Sonochemistry and Sonochemistry Followed by Hydrothermal Conventional Method, *Ultrason. Sonochem.*, 2019, **58**, 104620.

6 C. C. de Foggi, R. C. de Oliveira, M. T. Fabbro, C. E. Vergani, J. Andres, E. Longo and A. L. Machado, Tuning the Morphological, Optical, and Antimicrobial Properties of α-Ag_2WO_4 Microcrystals Using Different Solvents, *Cryst. Growth Des.*, 2017, **17**(12), 6239–6246.

7 M. Assis, E. Cordoncillo, R. Torres-Mendieta, H. Beltrán-Mir, G. Mínguez-Vega, R. Oliveira, E. R. Leite, C. C. Foggi, C. E. Vergani, E. Longo and J. Andrés, Towards the Scale-up of the Formation of Nanoparticles on α-Ag_2WO_4 with Bactericidal Properties by Femtosecond Laser Irradiation, *Sci. Rep.*, 2018, **8**(1), 1884.

8 C. J. Santos, F. M. Filho, F. L. Campos, C. A. de Ferreira, A. L. B. de Barros and D. C. F. Soares, Ag_2WO_4 Nanoparticles Radiolabeled with Technetium-99m: A Potential New Tool for Tumor Identification and Uptake, *J. Radioanal. Nucl. Chem.*, 2020, **323**(1), 51–59.

9 M. Assis, T. Robeldo, C. C. Foggi, A. M. Kubo, G. Mínguez-Vega, E. Condoncillo, H. Beltran-Mir, R. Torres-Mendieta, J. Andrés, M. Oliva, C. E. Vergani, P. A. Barbugli, E. R. Camargo, R. C. Borra and E. Longo, Ag Nanoparticles/α-Ag_2WO_4 Composite Formed by Electron Beam and Femtosecond Irradiation as Potent Antifungal and Antitumor Agents, *Sci. Rep.*, 2019, **9**(1), 9927.

10 L. F. da Silva, A. C. Catto, W. Avansi, L. S. Cavalcante, V. R. Mastelaro, J. Andrés, K. Aguir and E. Longo, Acetone Gas Sensor Based on α-Ag_2WO_4 Nanorods Obtained via a Microwave-Assisted Hydrothermal Route, *J. Alloys Compd.*, 2016, **683**, 186–190.

11 L. F. Da Silva, A. C. Catto, W. Avansi, L. S. Cavalcante, J. Andrés, K. Aguir, V. R. Mastelaro and E. Longo, A Novel

Ozone Gas Sensor Based on One-Dimensional (1D) α-Ag_2WO_4 Nanostructures, *Nanoscale*, 2014, **6**(8), 4058–4062.

12 A. F. Gouveia, R. A. Roca, N. G. Macedo, L. S. Cavalcante, E. Longo, M. A. San-Miguel, A. Altomare, G. S. da Silva and J. Andrés, Ag_2WO_4 as a Multifunctional Material: Fundamentals and Progress of an Extraordinarily Versatile Semiconductor, *J. Mater. Res. Technol.*, 2022, **21**, 4023–4051.

13 M. M. Mohamed, S. M. Syam and M. Khairy, Extremely Efficient Methanol Oxidation Reaction Performance: A Highly Active Catalyst Derived from Different $Mn_{2-X}O_y$ Phases-Supported Ag@Ag_2WO_4, *Electrochim. Acta*, 2023, **437**, 141528.

14 K. Nubla and N. Sandhyarani, Ag Nanoparticles Anchored Ag_2WO_4 Nanorods: An Efficient Methanol Tolerant and Durable Pt Free Electro-Catalyst toward Oxygen Reduction Reaction, *Electrochim. Acta*, 2020, **340**, 135942.

15 M. Farahmand Habibi and M. Arvand, A Novel and Durable Oxygen Reduction Reaction Catalyst with Enhanced Bio-Energy Generation in Microbial Fuel Cells Based on Ag/Ag_2WO_4@f-MWCNTs, *J. Electroanal. Chem.*, 2022, **926**, 116958.

16 Y. Song, W. Xie, C. Yang, D. Wei, X. Su, L. Li, L. Wang and J. Wang, Humic Acid-Assisted Synthesis of Ag/Ag_2MoO_4 and Ag/Ag_2WO_4 and Their Highly Catalytic Reduction of Nitro- and Azo-Aromatics, *J. Mater. Res. Technol.*, 2020, **9**(3), 5774–5783.

17 Q. W. Song, B. Yu, X. D. Li, R. Ma, Z. F. Diao, R. G. Li, W. Li and L. N. He, Efficient Chemical Fixation of CO2 Promoted by a Bifunctional Ag_2WO_4/Ph_3P System, *Green Chem.*, 2014, **16**(3), 1633–1638.

18 C. X. Guo, B. Yu, J. N. Xie and L. N. He, Silver Tungstate: A Single-Component Bifunctional Catalyst for Carboxylation of Terminal Alkynes with CO_2 in Ambient Conditions, *Green Chem.*, 2015, **17**(1), 474–479.

19 M. Assis, A. F. Gouveia, L. K. Ribeiro, M. A. Ponce, M. S. Churio, O. N. Oliveira, L. H. Mascaro, E. Longo, R. Llusar, E. Guillamón and J. Andrés, Towards an Efficient Selective Oxidation of Sulfides to Sulfonic by $NiWO_4$ and α-Ag_2WO_4, *Appl. Catal., A*, 2023, **625**, 119038.

20 L. O. Libero, L. K. Ribeiro, L. I. Granone, M. S. Churio, J. C. Souza, V. R. Mastelaro, J. Andrés, E. Longo, L. H. Mascaro and M. Assis, Introducing Structural Diversity: $Fe_2(MoO_4)_3$ Immobilized in Chitosan Films as an Efficient Catalyst for the Selective Oxidation of Sulfides to Sulfones, *ChemCatChem*, 2023, **15**(10), e202300421.

21 K. M. Borys, M. D. Korzyński and Z. Ochal, Derivatives of Phenyl Tribromomethyl Sulfone as Novel Compounds with Potential Pesticidal Activity, *Beilstein J. Org. Chem.*, 2012, **8**, 259–265.

22 X. Chen, S. Hussain, S. Parveen, S. Zhang, Y. Yang and C. Zhu, Sulfonyl Group-Containing Compounds in the Design of Potential Drugs for the Treatment of Diabetes and Its Complications, *Curr. Med. Chem.*, 2012, **19**(21), 3578–3604.

23 J. Choi, P. Martín-Gago and G. C. Fu, Stereoconvergent Arylations and Alkenylations of Unactivated Alkyl Electrophiles: Catalytic Enantioselective Synthesis of Secondary Sulfonamides and Sulfones, *J. Am. Chem. Soc.*, 2014, **136**(34), 12161–12165.

24 M. V. Kachaeva, D. M. Hodyna, I. V. Semenyuta, S. G. Pilyo, V. M. Prokopenko, V. V. Kovalishyn, L. O. Metelytsia and V. S. Brovarets, Design, Synthesis and Evaluation of Novel Sulfonamides as Potential Anticancer Agents, *Comput. Biol. Chem.*, 2018, **74**, 294–303.

25 M. Radko, M. Rutkowska, A. Kowalczyk, P. Mikrut, A. Święs, U. Díaz, A. E. Palomares, W. Macyk and L. Chmielarz, Catalytic Oxidation of Organic Sulfides by H_2O_2 in the Presence of Titanosilicate Zeolites, *Microporous Mesoporous Mater.*, 2020, **302**, 110219.

26 M. Muñoz, L. J. Mendoza-Herrera, G. P. Romanelli, D. Gazzoli and C. I. Cabello, Catalytic Behavior of the WO_x-ZrO_2 System in the Clean Selective Oxidation of Diphenyl Sulfide (DPS), *Catal. Today*, 2021, **372**, 146–153.

27 R. A. Sheldon, Metrics of Green Chemistry and Sustainability: Past, Present, and Future, *ACS Sustainable Chem. Eng.*, 2018, **6**(1), 32–48.

28 N. F. Andrade Neto, P. M. Oliveira, M. R. D. Bomio and F. V. Motta, Effect of Temperature on the Morphology and Optical Properties of Ag_2WO_4 Obtained by the Co-Precipitation Method: Photocatalytic Activity, *Ceram. Int.*, 2019, **45**(12), 15205–15212.

29 L. K. Ribeiro, A. F. Gouveia, F. C. M. das Silva, L. F. G. Noleto, M. Assis, A. M. Batista, L. S. Cavalcante, E. Guillamón, I. L. V. Rosa, E. Longo, J. Andrés and G. E. Luz Júnior, Tug-of-War Driven by the Structure of Carboxylic Acids: Tuning the Size, Morphology, and Photocatalytic Activity of α-Ag2WO4, *Nanomaterials*, 2022, **12**(19), 336.

30 N. G. Macedo, A. F. Gouveia, R. A. Roca, M. Assis, L. Gracia, J. Andrés, E. R. Leite and E. Longo, Surfactant-Mediated Morphology and Photocatalytic Activity of α-Ag_2WO_4 Material, *J. Phys. Chem. C*, 2018, **122**(15), 8667–8679.

31 W. D. S. Pereira, M. M. Ferrer, G. Botelho, L. Gracia, I. C. Nogueira, I. M. Pinatti, I. L. V. Rosa, F. D. A. La Porta, J. Andrés and E. Longo, Effects of Chemical Substitution on the Structural and Optical Properties of α-$Ag_{2-2x}Ni_xWO_4$ ($0 \leq x \leq 0.08$) Solid Solutions, *Phys. Chem. Chem. Phys.*, 2016, **18**(31), 21966–21975.

32 P. F. S. Pereira, C. C. Santos, A. F. Gouveia, M. M. Ferrer, I. M. Pinatti, G. Botelho, J. R. Sambrano, I. Rosa, J. Andrés and E. Longo, α-$Ag_{2-2x}Zn_xWO_4$ ($0 \leq x \leq 0.25$) Solid Solutions: Structure, Morphology, and Optical Properties, *Inorg. Chem.*, 2017, **56**(13), 7360–7372.

33 X. Tang, J. Li and J. Hao, Significant Enhancement of Catalytic Activities of Manganese Oxide Octahedral Molecular Sieve by Marginal Amount of Doping Vanadium, *Catal. Commun.*, 2010, **11**(10), 871–875.

34 X. Guo, M. Li, P. Zhao, X. Wang and Q. Tang, Vanadium Doped OMS-2 Catalysts for One-Pot Synthesis of Imine from Benzyl Alcohol and Aniline: Effects of Vanadium Content and Precursor, *Catal. Commun.*, 2022, **172**, 106540.

35 M. Radko, A. Kowalczyk, E. Bidzińska, S. Witkowski, S. Górecka, D. Wierzbicki, K. Pamin and L. Chmielarz, Titanium Dioxide Doped with Vanadium as Effective Catalyst for Selective Oxidation of Diphenyl Sulfide to Diphenyl Sulfonate, *J. Therm. Anal. Calorim.*, 2018, **132**(3), 1471–1480.

36 L. S. Cavalcante, M. A. P. Almeida, W. Avansi, R. L. Tranquilin, E. Longo, N. C. Batista, V. R. Mastelaro and M. S. Li, Cluster Coordination and Photoluminescence Properties of α-Ag_2WO_4 Microcrystals, *Inorg. Chem.*, 2012, **51**(20), 10675–10687.

37 A. Turkovič, D. L. Fox, J. F. Scott, S. Geller and G. F. Ruse, High Temperature Raman Spectroscopy of Silver Tetratungstate, $Ag_8W_4O_{16}$, *Mater. Res. Bull.*, 1977, **12**(2), 189–195.

38 S. K. Gupta, K. Sudarshan, P. S. Ghosh, S. Mukherjee and R. M. Kadam, Doping-Induced Room Temperature Stabilization of Metastable β-Ag_2WO_4 and Origin of Visible Emission in α- And β-Ag_2WO_4: Low Temperature Photoluminescence Studies, *J. Phys. Chem. C*, 2016, **120**(13), 7265–7276.

39 Z. Lin, J. Li, Z. Zheng, J. Yan, P. Liu, C. Wang and G. Yang, Electronic Reconstruction of Alpha-Ag_2WO_4 Nanorods for Visible-Light Photocatalysis, *ACS Nano*, 2015, **9**(7), 7256–7265.

40 I. M. Pinatti, T. G. Ireland, G. R. Fern, I. L. V. Rosa and J. Silver, Low Temperature Micro Raman and Laser Induced Upconversion and Downconversion Spectra of Europium Doped Silver Tungstate $Ag_{2-3x}Eu_xWO_4$ Nanorods, *J. Mater. Sci.: Mater. Electron.*, 2017, **28**(10), 7029–7035.

41 I. M. Pinatti, I. C. Nogueira, W. S. Pereira, P. F. S. Pereira, R. F. Gonçalves, J. A. Varela, E. Longo and I. L. V. Rosa, Structural and Photoluminescence Properties of Eu^{3+} Doped α-Ag_2WO_4 Synthesized by the Green Coprecipitation Methodology, *Dalton Trans.*, 2015, **44**(40), 17673–17685.

42 Y. D. Premchand and S. A. Suthanthiraraj, Structural Investigation of (CuI)0.45–(Ag_2WO_4)0.55 Solid Electrolyte Using X-Ray Photoelectron and Laser Raman Spectroscopies, *Electrochem. Commun.*, 2004, **6**(12), 1266–1269, DOI: 10.1016/j.elecom.2004.09.026.

43 P. Muthukumar, P. Nantheeswaran, M. Mariappan, M. Pannipara, A. G. Al-Sehemi and S. P. Anthony, F and Rare V^{4+} Doped Cobalt Hydroxide Hybrid Nanostructures: Excellent OER Activity with Ultralow Overpotential, *Dalton Trans.*, 2023, **52**(14), 4606–4615.

44 D. L. Wood and J. Tauc, Weak Absorption Tails in Amorphous Semiconductors, *Phys. Rev. B: Solid State*, 1972, **5**(8), 3144–3151.

45 P. Kubelka and F. Munk, Ein Beitrag Zur Optik Der Farbanstriche, *Zeitschrift fur technische Physik*, 1931, **12**, 593–601.

46 R. A. Roca, J. C. Sczancoski, I. C. Nogueira, M. T. Fabbro, H. C. Alves, L. Gracia, L. P. S. Santos, C. P. de Sousa, J. Andrés, G. E. Luz, E. Longo and L. S. Cavalcante, Facet-Dependent Photocatalytic and Antibacterial Properties of α-Ag_2WO_4 Crystals: Combining Experimental Data and Theoretical Insights, *Catal. Sci. Technol.*, 2015, **5**(8), 4091–4107.

47 A. S. Barnard and P. Zapol, A Model for the Phase Stability of Arbitrary Nanoparticles as a Function of Size and Shape, *J. Chem. Phys.*, 2004, **121**(9), 4276–4283.

48 C. Shen, W. Lin, H. Hu, P. Yang and L. Wang, The Electronic and Geometric Structure Modifications of $LiFePO_4$ with Vanadium Doping to Achieve Ultrafast Discharging Capability: The Experimental and Theoretical Investigations, *J. Alloys Compd.*, 2023, **936**, 168035.

49 V. M. Longo, L. S. Cavalcante, E. C. Paris, J. C. Sczancoski, P. S. Pizani, M. S. Li, J. Andrés, E. Longo and J. A. Varela, Hierarchical Assembly of $CaMoO_4$ nano-Octahedrons and Their Photoluminescence Properties, *J. Phys. Chem. C*, 2011, **115**(13), 5207–5219.

50 M. Assis, R. A. P. Ribeiro, M. H. Carvalho, M. M. Teixeira, Y. G. Gobato, G. A. Prando, C. R. Mendonça, L. de Boni, A. J. Aparecido de Oliveira, J. Bettini, J. Andrés and E. Longo, Unconventional Magnetization Generated from Electron Beam and Femtosecond Irradiation on α-Ag_2WO_4: A Quantum Chemical Investigation, *ACS Omega*, 2020, **5**(17), 10052–10067.

51 M. Assis, M. A. Ponce, A. F. Gouveia, D. Souza, J. P. de Campos da Costa, V. Teodoro, Y. G. Gobato, J. Andres, C. Macchi, A. Somoza and E. Longo, Revealing the Nature of Defects in α-Ag_2WO_4 by Positron Annihilation Lifetime Spectroscopy: A Joint Experimental and Theoretical Study, *Cryst. Growth Des.*, 2021, **21**, 1093–1102.

52 A. B. Trench, T. Machado, A. F. Gouveia, M. Assis, L. Trindade, C. Santos, A. Perrin, P. Christiane, M. Oliva, J. Andres and E. Longo, Connecting Structural, Optical, and Electronic Properties and Photocatalytic Activity of Ag_3PO_4:Mo Complemented by DFT Calculations, *Appl. Catal., B*, 2018, **238**, 198–211.

53 A. F. Gouveia, L. Gracia, E. Longo, M. A. San-Miguel and J. Andrés, Modulating the Properties of Multifunctional Semiconductors by Means of Morphology: Theory Meets Experiments, *Comput. Mater. Sci.*, 2021, **188**, 110217.

54 C. C. De Foggi, R. C. De Oliveira, M. Assis, M. T. Fabbro, V. R. Mastelaro, C. E. Vergani, L. Gracia, J. Andrés, E. Longo and A. L. Machado, Unveiling the Role of β-Ag_2MoO_4 Microcrystals to the Improvement of Antibacterial Activity, *Mater. Sci. Eng., C*, 2020, 110765.

55 M. Assis, C. C. de Foggi, V. Teodoro, J. P. de Campos da Costa, C. E. Silva, T. Robeldo, P. F. Caperucci, C. E. Vergani, R. C. Borra, I. Sorribes, A. F. Gouveia, M. A. San-Miguel, J. Andrés and E. Longo, Surface-Dependent Photocatalytic and Biological Activities of Ag_2CrO_4: Integration of Experiment and Simulation, *Appl. Surf. Sci.*, 2021, **545**, 148964.

56 G. Zhuang, Y. Chen, Z. Zhuang, Y. Yu and J. Yu, Oxygen Vacancies in Metal Oxides: Recent Progress towards Advanced Catalyst Design, *Sci. China Mater.*, 2020, **63**(11), 2089–2118.

57 M. Assis, M. S. Castro, C. M. Aldao, C. Buono, P. P. Ortega, M. D. Teodoro, J. Andrés, A. F. Gouveia, A. Z. Simões, E. Longo, C. E. Macchi, A. Somoza, F. Moura and

M. A. Ponce, Disclosing the Nature of Defects in α-Ag_2WO_4, *Mater. Res. Bull.*, 2023, **164**, 12252.

58 J. Jupille and G. Thornton, *Defects at Oxide Surfaces*, Springer, New York, 2015, Vol. 58.

59 I. Nakamura, N. Negishi, S. Kutsuna, T. Ihara, S. Sugihara and K. Takeuchi, Role of Oxygen Vacancy in the Plasma-Treated TiO_2 Photocatalyst with Visible Light Activity for NO Removal, *J. Mol. Catal. A: Chem.*, 2000, **161**, 205–212.

60 H. Trabelsi, M. Bejar, E. Dhahri, M. P. F. Graça, M. A. Valente, M. J. Soares and N. A. Sobolev, Raman, EPR and Ethanol Sensing Properties of Oxygen-Vacancies $SrTiO_{3-\delta}$ Compounds, *Appl. Surf. Sci.*, 2017, **426**, 386–390.

61 M. S. Castro, L. Perissinotti and C. M. Aldao, Cooling Rate Effects in ZnO Varistors, *J. Mater. Sci.: Mater. Electron.*, 1992, **3**, 218–221.

62 J. Qian, Z. Peng, Z. Shen, Z. Zhao, G. Zhang and X. Fu, Positive Impedance Humidity Sensors via Single-Component Materials, *Sci. Rep.*, 2016, **6**, 25574.

63 Z. Shen, Z. Zhao, J. Wen, J. Qian, Z. Peng and X. Fu, Role of Oxygen Vacancies in the Electrical Properties of WO_{3-x} Nano/Microrods with Identical Morphology, *J. Nanomater.*, 2018, 7802589.

64 C. Di Valentin and G. Pacchioni, Spectroscopic Properties of Doped and Defective Semiconducting Oxides from Hybrid Density Functional Calculations, *Acc. Chem. Res.*, 2014, **47**, 3233–3241.

65 V. Luca, S. Thomson and R. F. Howe, Spectroscopic Investigation of Vanadium Speciation in Vanadium-Doped Nanocrystalline Anatase, *J. Chem. Soc., Faraday Trans.*, 1997, **93**(12), 2195–2202.

66 S. Songara, M. K. Patra, M. Manoth, L. Saini, V. Gupta, G. S. Gowd, S. R. Vadera and N. Kumar, Synthesis and Studies on Photochromic Properties of Vanadium Doped TiO_2 Nanoparticles, *J. Photochem. Photobiol., A*, 2010, **209**, 68–73.

67 S. Liang, K. Hofman, M. Friedrich, J. Keller and G. Manolikakes, Recent Progress and Emerging Technologies towards a Sustainable Synthesis of Sulfones, *ChemSusChem*, 2021, **14**(22), 4878–4902.

68 F. Dulieu, M. Minissale and D. Bockelée-Morvan, Production of O2 through Dismutation of H_2O_2 during Water Ice Desorption: A Key to Understanding Comet O_2 Abundances, *Astron. Astrophys.*, 2017, **597**, 4–8.

69 D. I. Foustoukos, J. L. Houghton, W. E. Seyfried, S. M. Sievert and G. D. Cody, Kinetics of H_2–O_2–H_2O Redox Equilibria and Formation of Metastable H_2O_2 under Low Temperature Hydrothermal Conditions, *Geochim. Cosmochim. Acta*, 2011, **75**(6), 1594–1607.

70 J. Brame, M. Long, Q. Li and P. Alvarez, Trading Oxidation Power for Efficiency: Differential Inhibition of Photo-Generated Hydroxyl Radicals versus Singlet Oxygen, *Water Res.*, 2014, **60**, 259–266.